Biomedicine & Pharmacotherapy 195 (2026) 119036

Contents lists available at ScienceDirect

Biomedicine & Pharmacotherapy

journal homepage: www.elsevier.com/locate/biopha

CD44 receptor-driven graphene oxide based nanocarriers for cancer therapy

Ludmila Žárská [a,*], Michaela Gapčová [a,b], Zuzana Chaloupková [a], Václav Ranc [a,c,**]

[a] Regional Centre of Advanced Technologies and Materials, Czech Advanced Technology and Research Institute (CATRIN), Palacký University Olomouc, Slechtitelu 26, Olomouc 779 00, Czech Republic
[b] Department of Medical Biophysics, Faculty of Medicine and Dentistry, Palacký University Olomouc, Hněvotínská 3, Olomouc 779 00, Czech Republic
[c] Institute of Molecular and Translation Medicine, Faculty of Medicine and Dentistry, Palacký University in Olomouc, Hněvotínská 5, Olomouc CZ-779 00, Czech Republic

ARTICLE INFO

Keywords:
Targeted drug delivery
Anticancer therapy
Hyaluronic acid
Doxorubicin
CD44

ABSTRACT

Interactions between hyaluronic acid (HA) and the CD44 receptor represent a key mechanism in tumor cell recognition and selective drug uptake. In this study, we compare the efficacy of a graphene oxide (GO)-based nanoplatform in two cell lines with markedly different CD44 expression levels. The aim is to investigate how HA functionalization and its concentration influence the biological behavior of these GO nanocarriers designed for targeted delivery of doxorubicin (DOX). The nanoplatform was prepared by sequential PEGylation of nanosized GO, followed by HA conjugation at three concentrations (0.1, 1, and 10 mg/mL) and subsequent DOX loading. Spectroscopic and microscopic analyses confirmed stepwise surface modification, formation of a stable polymer coating, and successful DOX incorporation through π–π stacking and hydrogen bonding. Biological assays demonstrated that HA enhances CD44-mediated internalization and increases anticancer activity in $CD44^+$ HT-1080 cells, while the GO@PEG carrier alone showed minimal cytotoxicity, highlighting its good biocompatibility. In contrast, $CD44^-$ SKBR3 cells displayed limited uptake and higher viability, consistent with weaker HA–CD44 interactions and lower receptor expression. Confocal microscopy and Raman spectroscopy visualized effective intracellular accumulation and perinuclear localization of the nanocarrier, further confirming selective internalization mechanisms. Overall, the results provide important insight into the role of HA in improving the specificity, cellular uptake, and safety of GO-based nanoplatforms. The study underscores the significance of CD44 receptor levels in determining therapeutic efficiency and supports the development of receptor-targeted, biocompatible nanocarrier systems for precision cancer therapy.

1. Introduction

Cancer therapy remains a significant challenge due to the complexity of the disease, arising, among other factors, from tumor heterogeneity, and the limitations of traditional treatment methods, including chemotherapy and radiation [1–3]. Drug carriers have emerged as a transformative approach to enhance the efficacy, specificity, and safety of cancer treatments [3,4]. These carriers, which include nanoparticles, liposomes, dendrimers, micelles, and polymeric systems, enable targeted drug delivery, minimizing off-target effects and reducing systemic toxicity [5,6]. Surface modifications, such as PEGylation or ligand functionalization, allow for selective accumulation of therapeutic agents in tumor tissues through passive or active targeting mechanisms, including enhanced permeability and retention (EPR) effect or receptor-mediated uptake [7–9].

PEGylation was employed primarily to enhance nanoplatform stability and biocompatibility, while the key selectivity of the system is achieved through active targeting via hyaluronic acid-mediated CD44 receptor recognition [10–12]. Doxorubicin (DOX) is a widely used anthracycline chemotherapeutic agent whose anticancer activity is primarily based on DNA intercalation and inhibition of topoisomerase II, leading to impaired DNA replication and apoptosis. Despite its high therapeutic efficacy, the clinical application of DOX is limited by severe systemic toxicity, including cardiotoxicity and nonspecific uptake by

* Corresponding author.
** Corresponding author at: Regional Centre of Advanced Technologies and Materials, Czech Advanced Technology and Research Institute (CATRIN), Palacký University Olomouc, Slechtitelu 26, Olomouc 779 00, Czech Republic.
E-mail addresses: ludmila.zarska01@upol.cz (L. Žárská), vaclav.ranc@upol.cz (V. Ranc).

https://doi.org/10.1016/j.biopha.2026.119036
Received 4 December 2025; Received in revised form 14 January 2026; Accepted 21 January 2026
Available online 27 January 2026

healthy tissues. These limitations have motivated the development of targeted drug delivery strategies aimed at improving tumor selectivity while reducing off-target effects [13,14].

Receptor-mediated uptake targeting CD44 via specific interactions with hyaluronic acid (HA), which binds to this cell-surface receptor overexpressed in many types of cancer, represents a promising strategy in this area [15,16]. Hyaluronic acid, a naturally occurring glycosaminoglycan, selectively binds to CD44, facilitating targeted delivery of therapeutic agents to tumor cells. This approach takes advantage of the overexpression of CD44 on the surface of many tumor cells to enhance cellular uptake by serving as a primary binding site for HA, ensuring more selective and efficient drug accumulation in the tumor microenvironment [16,17]. The HA-CD44 axis has also shown potential to reduce systemic toxicity and improve pharmacokinetics [18].

The current study employed comparative in vitro analysis to determine the targeted drug delivery efficacy of the HA-functionalized GO nanoplatform against two distinct cancer cell lines possessing markedly different levels of CD44 surface expression. In particular, we developed a GO-based nanodrug delivery system functionalized with 8-arm PEG-NH_2 and HA for targeted delivery of DOX. The branched PEG architecture enhances stability and provides reactive sites for bioconjugation, while HA enables active targeting via the CD44 receptor, commonly overexpressed in various cancer cells. DOX was efficiently loaded onto the functionalized graphene oxide (GO) through non-covalent π–π interactions, preserving its bioactivity. The resulting nanoplatform – GO@PEG–HA–DOX was thoroughly characterized by atomic force microscopy (AFM), scanning electron microscopy (SEM), fourier transform infrared (FTIR) and ultraviolet–visible (UV-Vis) spectroscopy to confirm morphology and surface chemical functionalization. *In vitro* cytotoxicity was assessed on two human cancer cell lines - HT-1080 fibrosarcoma cells ($CD44^+$) and SKBR3 breast cancer cells ($CD44^-$) - using Alamar Blue and live/dead staining. To investigate cellular uptake pathways and verify intracellular localization of the nanocarrier, we employed confocal microscopy and Raman spectroscopy. These techniques were selected to enable precise visualization of nanoplatform internalization and its potential accumulation in cells.

2. Materials and methods

2.1. GO flake size optimization

Graphene oxide obtained from Sigma Aldrich (Saint Louis, MO, USA) was used as the initial material for this study. The adjustment and selection of flake sizes were performed using a combined methodology based on two previously documented protocols [19,20]. Initially, a GO stock solution (4 mg/mL) was diluted to a final concentration of 400 μg/mL using phosphate-buffered saline (PBS). This diluted solution was subjected to sonication in a Sonorex Digitec DT 103 H ultrasonic bath (Bandelin, Berlin, Germany) at 80°C for 6 h. Following this, the sample was agitated for 18 h using a Heidolph Unimax 1010 shaker (500 RPM, 65°C) from Heidolph (Schwabach, Germany) and then sonicated again in the ultrasonic bath at 80°C for another 6 h. Larger flakes were subsequently removed through centrifugation (Benchtop 4–16 K, 21, 191RCF, 10 min), leaving a supernatant containing the GO dispersion, which was utilized in all further experiments.

2.2. PEGylation of GO

A total of 25 mg of 8-arm PEG-NH_2 (10 kDa) from Sigma-Aldrich (St. Louis, MI, USA) was added to 5 mL of previously prepared GO dispersion. The mixture underwent a 10-min sonication process. Subsequently, 40 μL of N-(3-Dimethylaminopropyl)-N´-ethylcarbodiimide hydrochloride (EDC, Sigma-Aldrich) at a concentration of 5 mg/mL was added dropwise to the mixture. After 24 h of stirring (500 RPM, 65°C), a second round of stirring and sonication followed for 18 h (500 RPM, 65 °C) and 6 h (80 °C) respectively. Infrared spectra of the PEGylated GO were recorded using a Nicolet iS5 FTIR spectrometer (Fisher Scientific, Waltham, MA, USA) in ATR mode with a ZnSe crystal.

2.3. Hyaluronic acid

Hyaluronic acid (sodium salt of hyaluronic acid from rooster comb) from Sigma-Aldrich (St. Louis, MI, USA) was utilized at three concentrations: 0.1, 1 and 10 mg/mL. A stock solution of HA at 10 mg/mL was diluted to the indicated final concentration and added to 2 mL of pre-prepared GO@PEG and 8 μL of EDC (50 mg/mL). FTIR spectroscopy was employed to evaluate the presence of HA on the PEGylated GO nanoplatform. Spectra were recorded using a Nicolet iS5 FTIR spectrometer (Fisher Scientific, Waltham, MA, USA) in ATR mode with a ZnSe crystal.

2.4. DOX loading on GO@PEG_HA nanoplatforms

Doxorubicin (Sigma-Aldrich, St. Louis, MI, USA) was loaded onto the GO@PEG–HA nanoplatform via non-covalent π–π stacking interactions between the aromatic domains of doxorubicin and the graphene oxide surface. Briefly, a stock solution of DOX (10 mg/mL) was added to a defined amount of GO@PEG–HA dispersion to achieve a final DOX concentration of 214 μM. The mixture was stirred at room temperature (500 rpm) for 24 h to allow efficient adsorption of DOX onto the nanoplatform.

Following incubation, unbound DOX was removed by centrifugation at 21,191 RCF for 20 min. The concentration of DOX loaded onto the nanoplatform was determined by UV–Vis spectroscopy by measuring the absorbance of DOX in the supernatant. The loading efficiency (LE) was calculated according to a previously published method [21] as follows:

$$LE(\%) = \frac{\text{concentration of DOX loaded onto GO@PEG} - \text{HA}}{\text{initial concentration of DOX}} \text{x100}.$$

All measurements were performed in triplicate (N = 3). The resulting GO@PEG–HA–DOX pellet was gently resuspended in 1 mL of PBS. All samples were freshly prepared, and the DOX-loaded nanoplatforms were used immediately for subsequent biological experiments without prolonged storage.

2.5. Characterization of GO-based nanoplatforms

2.5.1. Determination of GO amount and size distribution

The concentration and size distribution of the nanoplatforms were evaluated according to a previously published protocol [22,23]. Graphene oxide flakes from the stock solution and the GO@PEG–HA–DOX nanoplatforms were analyzed to confirm morphological changes following functionalization. AFM measurements were performed using an Ntegra Spectra system (NT-MDT, Moscow, Russia) in semi-contact mode with ACTA-SS-10 tips at a scan rate of 0.3 Hz. A 5 μL aliquot of each sample was drop-cast onto freshly cleaved mica (0.5 cm radius) and air-dried at room temperature. The AFM height and size profiles were evaluated using *Gwyddion* and *ImageJ* software. The number and dimensions of GO flakes were analysed from 50 × 50 μm scan areas (N=1642). The resulting data were used to construct a size distribution histogram for GO@PEG–HA–DOX.

For complementary morphological characterization, scanning electron microscopy (SEM) images were obtained using a Hitachi SU6600 microscope (Hitachi, Tokyo, Japan). For pristine GO, a droplet of aqueous dispersion was deposited on a carbon tape and air-dried at room temperature. For GO@PEG–HA–DOX, a droplet of dispersion was applied onto a copper grid with a carbon support film and air-dried. Imaging was performed at accelerating voltages of 7 kV (GO) and 5 kV (GO@PEG).

2.6. In vitro biological study

2.6.1. Cell culture

For *in vitro* biological experiments, SKBR3 cells (a human epithelial cell line derived from breast carcinoma) and HT-1080 cells (a malignant tumor cell line of mesenchymal origin) were employed. The SKBR3 cell line exhibits very low to minimal expression of CD44 ($CD44^-$), whereas HT-1080 cells are characterized by high levels of CD44 expression ($CD44^+$). SKBR3 cells were cultivated in DMEM (Gibco), and HT-1080 cells in EMEM (Gibco), both supplemented with 10 % fetal bovine serum (FBS; Gibco), 1 % L-glutamine (Gibco), and 1 % penicillin/streptomycin solution (100 U/mL – 100 μg/mL; Gibco). All cell handling procedures were conducted under sterile conditions in a laminar flow hood. Cells were cultured at 37 °C in a humidified incubator with 5 % CO_2. For experimental procedures, cells were detached by trypsinization, centrifuged, and resuspended in an appropriate volume of culture medium. Cell numbers in suspension were determined using a BioRad TC10™ automated cell counter (Marshall Scientific, Hampton, NH, USA).

2.7. Cell viability (Alamar Blue) assay

Cells loaded with GO@PEG–HA–DOX nanoplatforms at concentrations of 2, 11 and 15 μM were incubated in a thermobox at 37 °C and 5 % CO_2. The applied DOX concentrations were defined relative to the amount of DOX bound to the nanoplatform and were selected to cover a broad biologically relevant range, enabling evaluation of dose-dependent cytotoxic effects. The same concentration ranges were applied consistently to free DOX controls to ensure comparability between experimental groups. After 24 and 72 h of incubation, DMEM was replaced with Alamar blue solution (10 % of the total volume of medium in the well). The resazurin-based oxidation-reduction indicator Alamar blue was metabolized by living cells to fluorescent resorufin during 6 h of incubation at 37°C and 5 % CO_2 (this reaction does not occur in dead cells). The absorbance of the solution was evaluated by measuring in a 96-well multi-well reader (Tecan infinite M200 pro), at an emission wavelength of 590 nm (excitation 530–560 nm). Cell viability was subsequently calculated from the measured values, as the ratio of the average absorbance of the cell sample containing the tested compounds to the average absorbance of the control cells. The result of the Alamar Blue assay was reported as a percentage of cell viability, supplemented by the standard deviation from 6 different measurements.

2.8. Live & dead cytotoxicity assay

Live & Dead cytotoxicity assay is widely used to assess cell viability, commonly using calcein AM and propidium iodide (PI). Nonfluorescent calcein AM, a cell-permeable dye, is converted into green fluorescent calcein by intracellular esterases in viable cells, while dead cells remain nonfluorescent. In contrast, PI stains only non-viable cells by intercalating into nuclear DNA, emitting red fluorescence. Briefly, 10 000 HT-1080 and SKBR3 cells were seeded per well in a 96-well plate. The next day were cells treated with free DOX; GO@PEG–$HA_{0.1}$; GO@PEG–HA_1 and GO@PEG–HA_{10}, corresponding to a final DOX concentration of 15 μM for 24 and 72 h. Cell viability was assessed by calcein AM and PI. Cells were incubated with 1 μL of calcein AM (Invitrogen, USA) diluted in DMSO (50 μM) and 1 μL of PI (1 μg/mL, Sigma-Aldrich, USA) for 5 min. The culture medium was then replaced with 50 μL of warm PBS. Fluorescence was observed using an Olympus IX 70 fluorescence microscope (Olympus, Japan), and images were captured with a Quick Photo Camera 3.0 (Promicra, Czech Republic).

2.9. Confocal microscope imaging

Confocal microscopy is a non-invasive and non-destructive imaging technique that provides higher resolution and contrast compared to conventional light microscopy. It was used to track the intracellular localization of the tested materials, including DOX. To facilitate their visualization within the cells, cell membranes were stained with CellMask Deep Red, and nuclei were stained with Hoechst 33342 dye. The red fluorescence of DOX allowed for the assessment of its distribution within the cellular compartments.

For imaging, 30 000 cells per well were seeded into an 8-well confocal microscopy plate with 300 μL of culture medium and incubated for 24 h. The next day, cells were treated with GO@PEG–$HA_{0.1}$; GO@PEG–HA_1 and GO@PEG–HA_{10}, corresponding to a final DOX concentration of 15 μM. After 24 h incubation were cells washed with 300 μL of PBS and then incubated with CellMask Deep Red (5 mg/mL, Invitrogen, USA) at a final concentration of 5 μg/mL in culture medium for 5–10 min at 37 °C. Following incubation, the cells were washed three times with 300 μL of PBS, and 300 μL of fresh medium was added. Subsequently, 0,3 μL of Hoechst dye (1 mg/mL, Invitrogen, USA) was added, followed by a 5 min incubation. After staining, the medium was aspirated, and cells were washed with 300 μL of PBS. Finally, 300 μL of fresh culture medium was added, and the plate was placed in the confocal microscope for imaging. Fluorescence signals, including the intrinsic red fluorescence of doxorubicin, were captured using a confocal microscope Zeiss LSM 980 (Zeiss, Germany), and images were analyzed with Zen 2.3 software (Zeiss, Germany).

2.10. Fixation of cells for raman spectroscopy

To complement and validate the fluorescence microscopy results, Raman spectroscopy was employed as an additional label-free technique for the characterization of cellular responses to the tested nanomaterials. This method provides molecular-level insights into cellular composition and can reveal changes induced by nanoparticle uptake and intracellular interactions.

For this purpose, sterile glass coverslips were placed into a 24-well culture plate prior to cell seeding. Subsequently, 30,000 cells were seeded onto each coverslip in 500 μL of complete culture medium and incubated for 24 h. The next day, cells were treated with GO@PEG–HA–DOX at a concentration corresponding to 2 μM final DOX content. Following a 24-h incubation period, the coverslips were washed three times with 1 mL of PBS to remove residual medium and unbound material. Cells were then fixed at room temperature for 30 min using 1 mL of fixative solution composed of 1.5 % paraformaldehyde (4 % in PBS, Thermo Fisher Scientific, USA), 0.1 % glutaraldehyde (Sigma Aldrich, USA), and PBS. After fixation, the samples were washed once more with 1 mL of PBS and subsequently rinsed three times with 1 mL of distilled water to remove salts and minimize spectral background. Finally, the coverslips were air-dried at room temperature and stored in a dust-free environment until Raman analysis.

2.11. Raman spectroscopy

To detect the Raman signal of GO-based nanoplatform within cells, Raman spectral data were obtained on a DXR3 Raman microscope (Thermos Scientific) with an excitation laser operating at a wavelength of (532 nm or 785 nm, depending on which laser gives better results). Raman spectra were measured in the range from 500 to 3500 cm^{-1}. The spectral resolution of the laser and optics combination used was 1.0 cm^{-1}. The step size of the X and Y axes was no greater than 1 μm, which enabled high resolution. The range of movement in the Z axis was not limited, but allowed focusing on a sample with a maximum height of at least 5 mm. The experimental parameters were as follows; the number of accumulations was 32, with an exposure time of 2 s per accumulation, the laser power on a sample surface was 5 mW. A lens with 50 × magnification (with N.A. −0.55) was selected. A 50 μm pinhole assembly with a 1200 grooves per mm grid was selected in front of the CCD detector. Fluorescence correction was also enabled to remove unwanted fluorescence from the cells. The obtained spectra were then

adjusted to the baseline using OMNIC 8.2.0.403 software (polynomial approximation, where n = 3).

The distribution of the nanoplatform after interaction with cells was evaluated using Raman hyperspectral imaging. During mapping, an area of 2–4 cells (typically 100 × 130 μm) with a spatial resolution of 1 μm. Each spectrum in the map is represented by 8 averaged microscans, and the exposure time was 1 s. The spectra were evaluated using Project 5 software. First, cosmic noise was removed, followed by an ALS-based background correction and data smoothing using Sawitsky-Golay approach with a window size of 7. Resulting maps were obtained by univariate analysis targeted at basic characteristic Raman bands of GO (D and G bands) and cell compartments (proteins, lipids).

2.12. Statistical analysis

All measured values were initially assessed for outliers using Z-score analysis. Subsequently, the mean and standard deviation (SD) were calculated. Cell viability data were analysed using GraphPad Prism (version 8.0) via a two-way analysis of variance (ANOVA), followed by Dunnett's and Tukey's multiple comparison tests, where appropriate. Data are presented in graphs as mean ± standard deviation (SD). Statistical significance is indicated as follows: *P ≤ 0.05; **P ≤ 0.01; ***P ≤ 0.001; ****P ≤ 0.0001.

3. Results and discussion

Graphene oxide was employed as a two-dimensional carrier to construct multifunctional nanostructures for receptor-targeted delivery of DOX. The nanoplatform was rationally designed by integrating a GO core, a PEG shell, and an outer HA corona.

This configuration combines the structural and adsorption properties of GO, the steric stabilization and hydrophilicity conferred by PEG, and the CD44-mediated targeting capability of HA [12,13,15,16]. The resulting GO@PEG–HA–DOX nanostructures were thoroughly characterized to confirm successful surface modification, structural integrity, and effective DOX incorporation prior to biological testing.

3.1. Characterization of GO-based nanoplatforms

Commercially available GO was used as the base material for all dispersion preparations. The as-received GO consisted of large, polydisperse flakes typically exceeding several micrometres in lateral dimension. Such large flakes are not fully optimized for biological applications due to their limited dispersibility, reduced colloidal stability, and hindered cellular internalization [24–26]. To tailor the flake size towards the nanoscale regime and improve dispersion homogeneity, a combination of ultrasonic treatment and elevated temperature was applied, as described in 2.1, following adaptations of previously published protocols [19,20].

A stock suspension of GO (4 mg/mL) was diluted to 400 μg/mL in PBS and subjected to sequential ultrasonic and thermal processing. This treatment effectively induced exfoliation and fragmentation of the GO sheets, resulting in a substantial reduction of flake size while preserving the oxygen-containing functional groups essential for further modification. Larger aggregates were removed by triple centrifugation (21,191 RCF, 10 min), and the supernatant containing the purified GO fraction was collected for subsequent use.

AFM analysis confirmed a pronounced reduction in GO flake dimensions compared with the starting material. The pristine GO exhibited an average lateral size of approximately 5.4 μm and a thickness of 112.6 nm, corresponding to multilayer stacking (Supplementary Figure S1A, B). After ultrasonic processing, the flakes were significantly reduced to an average lateral dimension of 92.3 nm and a thickness of 1.1 nm, indicating successful exfoliation into one- to two-layer GO sheets (Supplementary Figure S1C, D) [21,23]. Following PEGylation, the lateral size of flakes increased slightly to 332 nm, and the thickness reached 41 nm, consistent with the formation of a polymer coating on the GO surface (Supplementary Figure S1E, F).

In the final GO@PEG–HA–DOX nanoplatform, the AFM images displayed uniform nanosheets with a mean lateral dimension of ~400 nm and a measured height of 68.9 nm (Fig. 1A–B). The corresponding height profile confirmed the consistent nanoscale morphology. This stepwise structural evolution from micrometre-sized pristine GO to nanometre-sized functionalized flakes demonstrates the effectiveness of the ultrasonic and thermal fragmentation process and subsequent PEGylation. Such morphology is highly advantageous for biological applications, promoting homogeneous surface functionalization, stable aqueous dispersion, and enhanced cellular interactions [27].

Complementary SEM imaging (Fig. 1D–E) supported the AFM observations, revealing a clear morphological transition from large, wrinkled sheets in the pristine GO to smaller, well-dispersed flakes after size refinement and PEG functionalization. The SEM images also confirmed the characteristic lamellar texture of GO, with overlapping edges indicative of exfoliated, thin-layer structures. Together, AFM and SEM analyses validate the successful preparation of well-dispersed, nanoscale GO-based materials suitable for further surface modification and biological evaluation.

Following PEGylation, HA was covalently conjugated to the GO@PEG surface at three concentrations (0.1, 1, and 10 mg/mL), and the resulting platform was subsequently loaded with DOX to yield the final GO@PEG–HA–DOX nanoplatform. AFM analysis revealed an additional increase in thickness to 68 nm and lateral dimensions of approximately 400 nm. After processing, 88 % of the analysed flakes (n = 1642) had lateral dimensions below 400 nm, confirming successful fractionation and functionalization (Fig. 1C). The full size distribution and height profiles are provided in Supplementary Figure S2.

3.2. Physicochemical characterization of GO-based nanoplatforms

Spectroscopic analysis confirmed the successful surface modification of GO and the incorporation of DOX into the final GO@PEG–HA–DOX nanoplatform (Fig. 2A–B). The obtained spectra demonstrated the stepwise functionalization of the GO surface, verifying the efficiency of PEG and HA grafting as well as the stability of the loaded drug. The combination of FTIR, UV–Vis and Raman spectroscopic techniques provided complementary information on the chemical interactions and structural transitions occurring during the formation of the multifunctional nanoplatform.

In the FTIR spectra (Fig. 2A), pristine GO showed characteristic bands of oxygen-containing groups, including O–H (~3400 cm^{-1}), C═O (~1720 cm^{-1}, label 2), C═C (~1580 cm^{-1}, label 3), and C–O–C (~1204 cm^{-1}). After carboxylation, a new –CH_2– stretching band appeared at ~2880 cm^{-1} (label 1). PEGylation with 8-arm PEG-NH_2 was confirmed by the emergence of an amide-carbonyl band at ~1650 cm^{-1} , together with reduced intensities of C═O- and C–O–related signals, consistent with covalent PEG attachment (Supplementary Figure S3) [27–29]. The subsequent conjugation of HA introduced additional characteristic peaks at 1 610 cm^{-1} and 1 410 cm^{-1} , corresponding to the asymmetric and symmetric stretching vibrations of carboxylate (COO^-) groups in HA [30]. These bands, together with a shift in the hydroxyl stretching region, indicated the formation of hydrogen bonds and electrostatic interactions between HA and the PEGylated GO surface. Following DOX loading, new absorption features appeared in the regions typically associated with C–N and C═O and C-H vibrations of DOX (Label 4), confirming its presence on the GO surface. These spectral changes support successful DOX association through π–π stacking and hydrogen-bonding interactions with the GO basal plane and the HA-modified surface.

The UV–Vis spectra (Fig. 2B) further confirmed the formation of the GO@PEG–HA–DOX nanoplatform. Pristine GO exhibited a typical absorption maximum at 230 nm, associated with π–π* transitions of aromatic C═C bonds, and a shoulder near 300 nm corresponding to n–π*

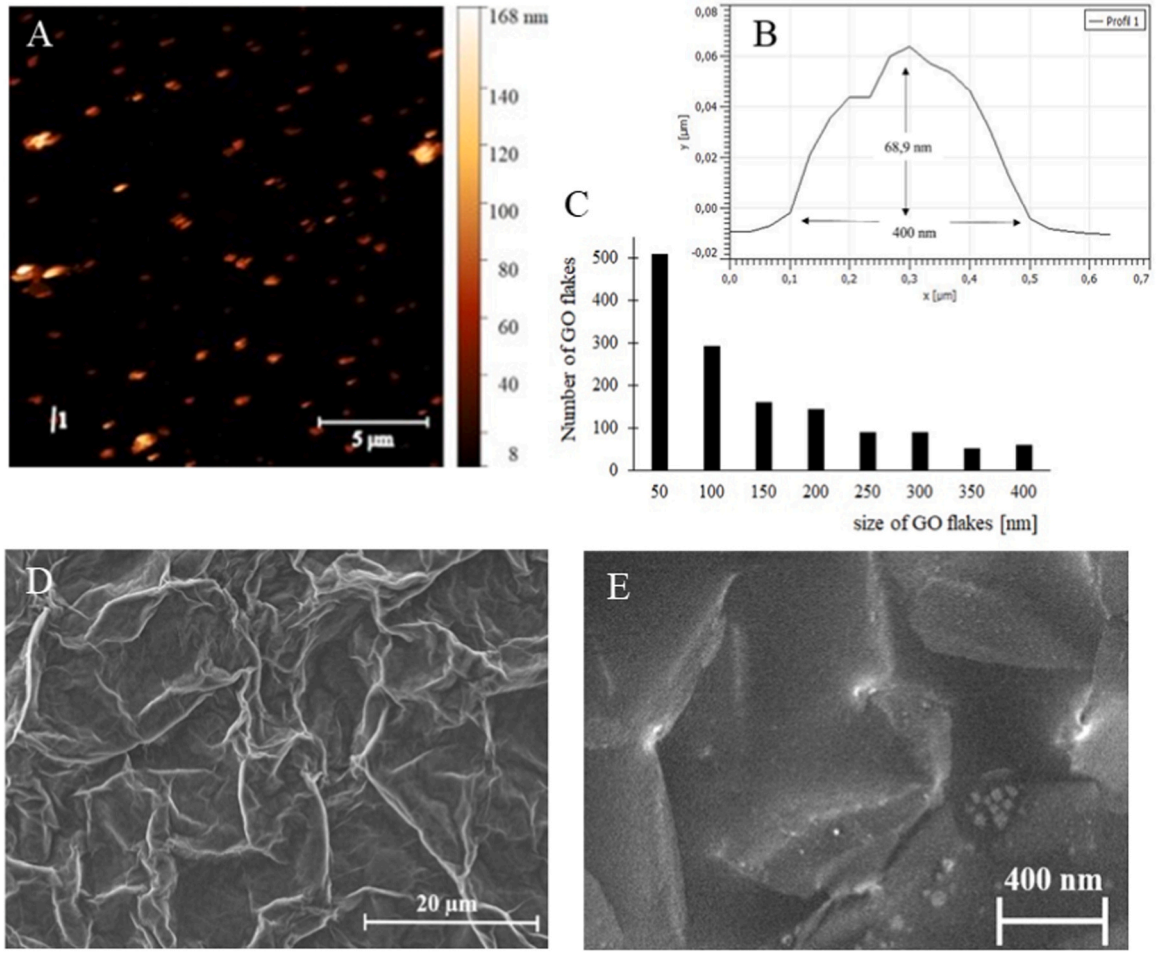

Fig. 1. Morphological characterization of GO-based nanoplatforms. (A) AFM images of GO@PEG–HA–DOX nanoplatforms. (B) Height profiles corresponding to the marked graphene oxide flakes. (C) Size distribution of graphene oxide flakes determined from the supernatant. (D) SEM image of graphene oxide in stock solution. (E) SEM image of PEGylated graphene oxide.

transitions of C═O bonds [31]. After PEG and HA modification, the intensity of these peaks slightly decreased, reflecting partial masking of the aromatic structure due to polymer coating. The spectrum of free DOX showed a prominent absorption band at 480 nm, attributed to the π–π* transition within the anthracycline chromophore [32]. In the GO@PEG–HA–DOX system, the characteristic absorption band of DOX was retained and exhibited a slight red shift relative to free DOX, consistent with π–π stacking and other non-covalent interactions between DOX and the GO surface. Such red-shift behaviour is commonly attributed to charge-transfer interactions between the aromatic domains of GO and the anthracycline chromophore of DOX, confirming molecular-level association of the drug with the nanocarrier.

Quantitative UV–Vis analysis revealed that, regardless of HA concentration (0.1, 1, and 10 mg/mL), the final amount of bound DOX was identical, corresponding to 22.6 µM and the LE = 11 %. This result suggests that the available binding sites on the GO@PEG–HA surface were fully saturated even at the lowest HA concentration, indicating reproducible and concentration-independent drug loading. Such efficient and uniform incorporation of DOX is consistent with previous reports on GO-based drug carriers, where π–π stacking and hydrogen bonding dominate the adsorption process [33].

The combined FTIR and UV–Vis data thus confirm the successful preparation of a GO-based nanoplatform with stepwise PEG and HA surface modification and efficient DOX incorporation. These findings validate the structural integrity and chemical stability of the developed GO@PEG–HA–DOX system, supporting its potential use as a multifunctional nanocarrier for targeted and controlled drug delivery.

The Raman spectra (Fig. 2C) show the characteristic bands of GO, with the D band (~1350 cm^{-1}) and G band (~1590 cm^{-1}). After PEG, HA, and DOX functionalization, an increase in intensity and in the I_D/I_G ratio was observed, indicating the introduction of additional defects and partial disruption of sp^2 domains due to surface modification. A slight red shift of the G band further suggests charge transfer between DOX and the graphene surface, confirming π–π interactions and successful functionalization of GO [34,35].

3.3. Cytotoxic evaluation of DOX-loaded GO@PEG–HA nanoplatforms

To evaluate the therapeutic potential and selectivity of the developed nanoplatform, the cytotoxic and biological effects of DOX-loaded GO@PEG–HA were investigated using two cancer cell lines with distinct CD44 expression profiles - HT-1080 and SKBR3. The design of this system was based on the hypothesis that HA functionalization would enable receptor-mediated targeting through specific interaction with CD44 receptors overexpressed on the surface of certain tumor cells, thereby promoting enhanced drug internalization and improved therapeutic efficacy.

The study focused on assessing the influence of DOX concentration, nanocarrier loading, and exposure time on cell viability, providing insight into both the targeting efficiency of the HA-functionalized PEGylated graphene oxide platform and the inherent cytotoxic properties of the encapsulated drug. The experiments were designed to capture

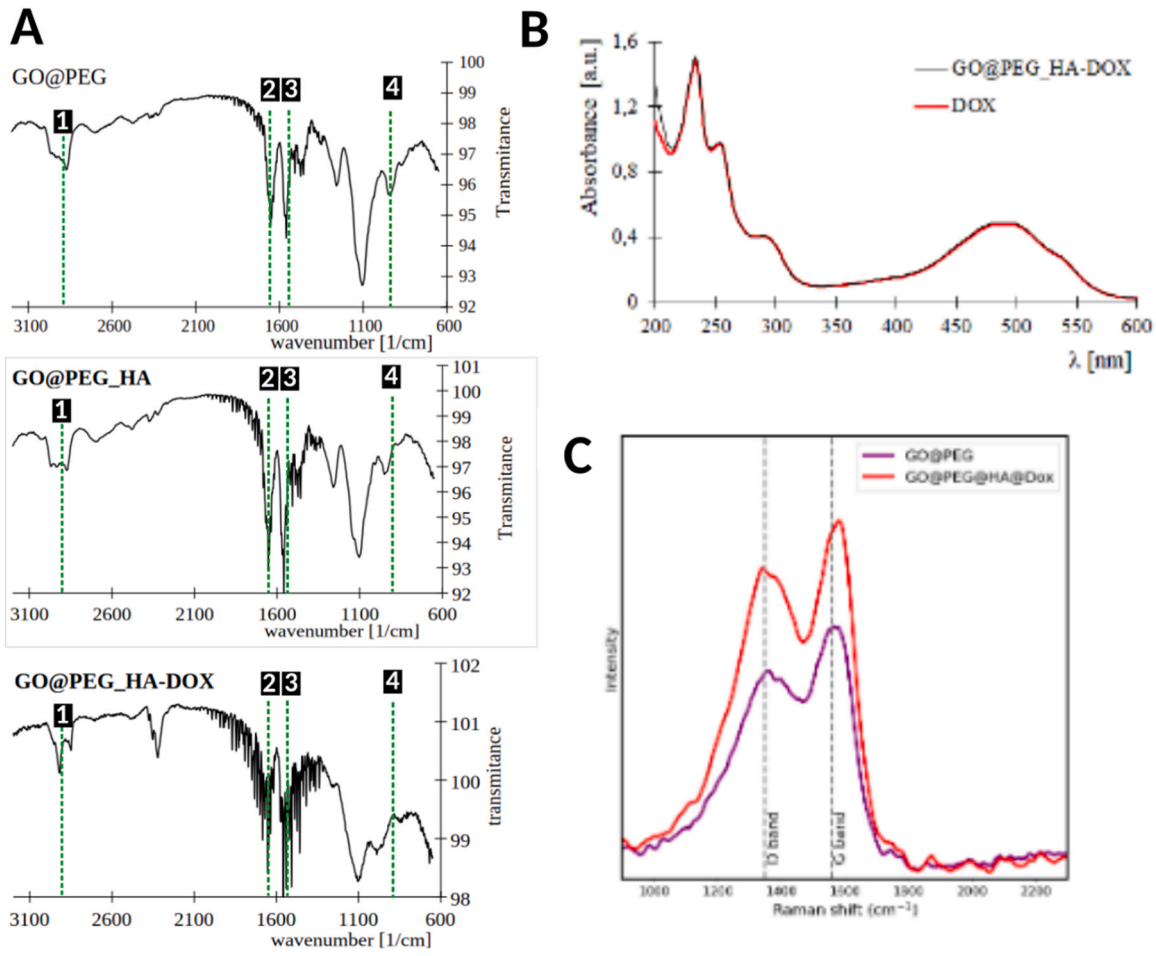

Fig. 2. Physicochemical characterization of GO@PEG–HA and GO@PEG–HA–DOX nanoplatforms with HA concentration 1 mg/mL. (A) FTIR spectra confirming successful PEGylation, HA functionalization, and DOX loading. Labels for functional groups 1: ν(C-H), 2: (-C═O), 3: (-C═O), 4:(-C-H) (B) UV–Vis spectra of GO@PEG–HA–DOX nanoplatforms showing characteristic absorption bands of DOX. (C) Raman spectra of GO-based nanoplatforms displaying characteristic D (~1350 cm^{-1}) and G (~1590 cm^{-1}) bands of GO.

the dynamics of DOX release and uptake over time (24 h and 72 h) and to distinguish between receptor-mediated effects and nonspecific cytotoxic mechanisms. By comparing two biologically distinct cell models, the study aimed to validate the role of CD44 in mediating HA–nanocarrier interactions and to confirm whether the GO@PEG–HA system could serve as an effective and biocompatible nanocarrier for selective delivery of doxorubicin in CD44-overexpressing tumors.

The cytotoxic response of DOX-loaded GO@PEG–HA nanoplatforms

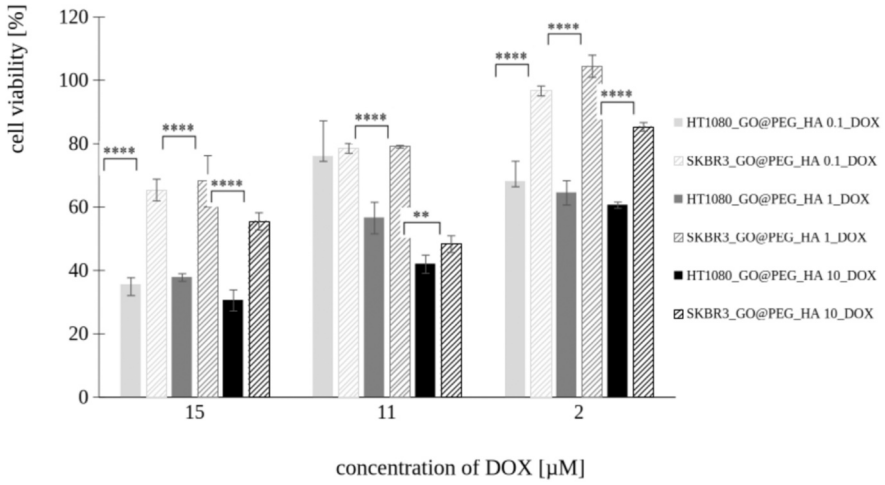

Fig. 3. Cell viability of HT-1080 and SKBR3 cells after 24 h exposure to DOX-loaded GO@PEG–HA nanoplatforms at different HA loadings (0.1, 1, and 10 mg/mL) and DOX concentrations (2, 11, and 15 μM).Data are presented in graphs as mean ± standard deviation (SD). Statistical significance is indicated as follows: *P ≤ 0.05; **P ≤ 0.01; ***P ≤ 0.001; ****P ≤ 0.0001.

was evaluated in two human cancer cell lines exhibiting distinct CD44 expression levels HT-1080 and SKBR3 to assess the influence of receptor-mediated targeting on drug efficacy. Both cell lines were treated with three concentrations of DOX (2, 11, and 15 μM) for 24 h and 72 h, using nanocarriers GO@PEG containing different HA loadings (0.1, 1, and 10 mg/mL).

After 24 h of exposure (Fig. 3), both cell lines showed a concentration-dependent decrease in viability, yet the magnitude of cytotoxicity varied significantly between them. The HT1080 cells, characterized by elevated CD44 expression, exhibited markedly reduced viability compared to SKBR3, particularly at higher DOX concentrations. At 15 μM DOX, HT1080 viability dropped below 40 %, while SKBR3 remained above 60 %. Similar trends were observed at 11 μM DOX, with HT-1080 cells retaining only 45–55 % viability compared to 50–80 % in SKBR3. At the lowest concentration (2 μM DOX), SKBR3 cells largely preserved viability (up to 100 %), whereas HT1080 viability decreased to approximately 60–70 %. These findings clearly indicate a selective cytotoxic effect toward CD44-overexpressing cells, suggesting efficient receptor-mediated uptake of HA-functionalized nanocarriers. Increasing the GO@PEG–HA ratio enhanced the cytotoxicity, confirming that higher HA surface density facilitates improved interaction with CD44 receptors and subsequent internalization. The higher cytotoxicity observed for HT-1080 cells at increased HA content was attributed to enhanced CD44–HA interactions promoting receptor-mediated uptake. This explanation has been added to the Discussion section in direct relation to the 24 h cytotoxicity data shown in Fig. 3.

Prolonging the exposure to 72 h (Fig. 4) led to a further overall reduction in cell viability, consistent with the time-dependent pharmacodynamics of DOX. At the highest concentration (15 μM DOX), both cell lines reached comparable viability levels (~35–40 %), suggesting that prolonged exposure and cumulative DOX diffusion reduced the selectivity observed at earlier time points. In contrast, at lower DOX concentrations (2–11 μM), SKBR3 cells consistently retained higher viability (50–80 %) compared to HT-1080 (40–55 %), demonstrating that CD44-mediated uptake remains dominant when the system operates under sub-saturating conditions.

The difference in cellular response between the two models is closely related to their CD44 receptor expression profiles. The CD44–HA interaction plays a central role in receptor-mediated endocytosis, facilitating the internalization of HA-decorated nanocarriers. In the case of HT1080 cells, abundant CD44 expression enables efficient binding and uptake of HA-functionalized GO@PEG, leading to higher intracellular DOX accumulation and enhanced cytotoxicity. Conversely, the SKBR3 cells, which express minimal CD44, exhibit limited receptor interaction, resulting in weaker uptake and reduced DOX-induced damage.

At prolonged incubation and higher DOX doses, nonspecific mechanisms such as passive diffusion across the plasma membrane become more dominant, explaining the convergence in viability between both cell lines after 72 h at 15 μM DOX. This suggests that while receptor targeting enhances early drug delivery and selectivity, the intrinsic cytotoxicity of DOX eventually overrides this specificity upon sustained exposure. Nonetheless, the persistent difference at lower concentrations indicates that CD44-mediated targeting remains an effective strategy for improving therapeutic selectivity under physiological conditions where drug doses are limited to reduce systemic toxicity.

Importantly, unloaded GO@PEG exhibited negligible cytotoxicity in both cell lines (viability $\geq$ 80–100 %), confirming its biocompatibility and suitability as a drug delivery vehicle (Figure S4). Overall, these results highlight that the combination of PEGylated GO and HA functionalization provides a powerful platform for selective, receptor-targeted delivery of doxorubicin to CD44-overexpressing tumor cells. The study further emphasizes the importance of optimizing the ratio between DOX concentration, nanocarrier loading, and exposure time to balance therapeutic efficacy with targeting selectivity.

3.4. Live dead assay

Fluorescence microscopy was employed to qualitatively assess cell viability using a dual-staining approach. Live cells were stained with Calcein-AM, which produces green fluorescence upon enzymatic conversion by intracellular esterases, whereas dead cells were labeled with propidium iodide, emitting red fluorescence after binding to nuclear DNA in membrane-compromised cells. Imaging was performed for untreated control cells, cells exposed to free DOX, and cells treated with GO@PEG–HA–DOX nanostructures. The carrier formulations were evaluated at three HA concentrations (0.1, 1, and 10 mg/mL), while the DOX concentration was kept constant at 15 μM across all treated samples to ensure direct comparison of cytotoxic effects.

Live/Dead fluorescence imaging after 24 h exposure revealed striking differences in the cytotoxic response of $CD44^+$ HT-1080 (Fig. 5A - E) and $CD44^-$ SKBR3 (Fig. 5F - J) cells to free and nanocarrier-bound DOX. Untreated controls (Fig. 5A, F) of both lines exhibited nearly exclusive green fluorescence, confirming high baseline viability.

In HT-1080 ($CD44^+$) cells (Fig. 5B), free DOX produced only moderate cytotoxicity, while HA-functionalized GO@PEG–HA–DOX formulations induced a progressive increase in cell death. The

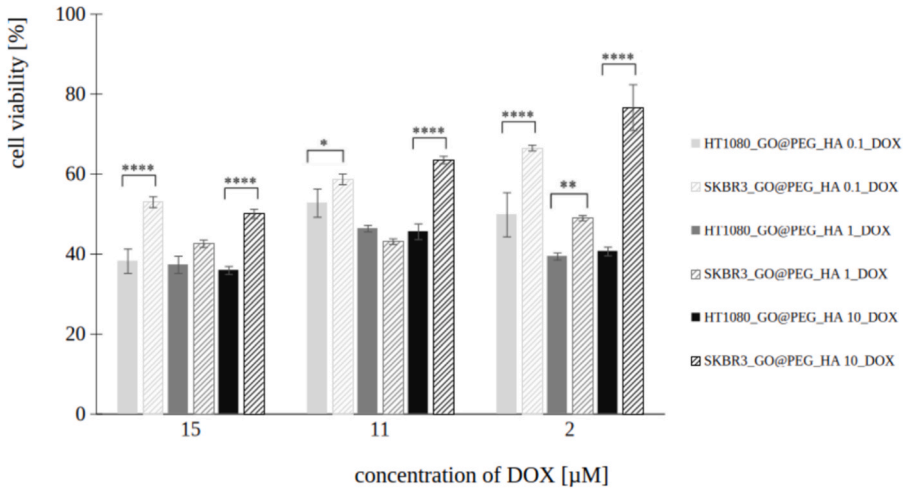

Fig. 4. Cell viability of HT-1080 ($CD44^+$) and SKBR3 ($CD44^-$) cells after 72 h incubation with DOX-loaded GO@PEG–HA nanoplatforms at different HA loadings (0.1, 1, and 10 mg/mL) and DOX concentrations (2, 11, and 15 μM). Data are presented as mean ± standard deviation (SD). Statistical significance is indicated as follows: *P $\leq$ 0.05; **P $\leq$ 0.01; ***P $\leq$ 0.001; ****P $\leq$ 0.0001.

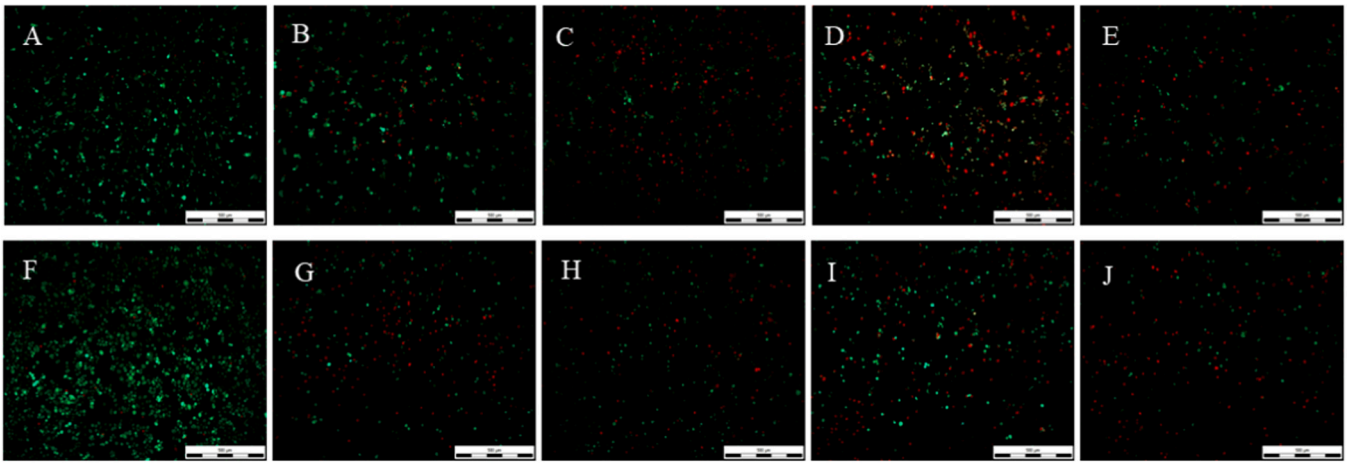

Fig. 5. Representative fluorescence microscopy images illustrating the viability of HT-1080 (A–E) and SKBR3 (F–J) cells following 24 h of incubation under different conditions. Green fluorescence (Calcein-AM) marks viable cells, whereas red fluorescence (propidium iodide) identifies non-viable cells. Control samples correspond to untreated cells, while all treated groups received DOX—free or GO@PEG–HA-bound—at a fixed concentration of 15 μM. The GO@PEG–HA carrier was tested at three HA concentrations (0.1, 1, and 10 mg/mL). HT-1080: (A) control, (B) free DOX, (C) GO@PEG–$HA_{0.1}$–DOX, (D) GO@PEG–HA_1–DOX, (E) GO@PEG–HA_{10}–DOX. SKBR3: (F) control, (G) free DOX, (H) GO@PEG–$HA_{0.1}$–DOX, (I) GO@PEG–HA_1–DOX, (J) GO@PEG–HA_{10}–DOX. Scale bar: 500 μm.

GO@PEG–HA_1–DOX treatment yielded the highest red fluorescence signal, indicating the strongest cytotoxic effect, consistent with efficient HA–CD44-mediated uptake and intracellular DOX release. Excessive HA decoration (GO@PEG–HA_{10}–DOX) resulted in a partial loss of efficacy, likely due to steric hindrance that limited nanoparticle internalization.

In contrast, SKBR3 ($CD44^-$) cells exhibited a different response pattern. A high proportion of red-stained cells was observed after exposure to free DOX, suggesting pronounced cytotoxicity within 24 h. The HA-functionalized nanocarriers (GO@PEG–$HA_{0.1}$–DOX, GO@PEG–HA_1–DOX, and GO@PEG–HA_{10}–DOX) produced a qualitatively similar or slightly reduced level of cell death compared to free DOX. Although the differences are not pronounced, this trend may indicate that in SKBR3 cells lacking CD44 receptors, HA decoration does not provide an additional cytotoxic advantage.

After 72 h of exposure, the overall proportion of dead cells increased markedly in both lines, but the differences between formulations became more pronounced. In HT-1080 cells (Fig. 6A-E), GO@PEG–HA_1–DOX remained the most effective treatment, consistent with efficient receptor-mediated uptake and sustained drug release. In SKBR3 cells (Fig. 6F-J), free DOX continued to elicit the strongest cytotoxic response, whereas the HA-coated nanocarriers induced similar but slightly attenuated effects. These qualitative differences suggest that HA functionalization enhances the cytotoxic efficacy primarily in CD44-rich environments, while its contribution in CD44-deficient cells remains limited.

Taken together, these findings indicate that both exposure time and receptor expression critically influence the therapeutic performance of GO@PEG–HA–DOX systems. The optimal HA coverage (HA_1) maximizes cytotoxic efficiency through balanced ligand density and cellular uptake in $CD44^+$ cells, whereas in $CD44^-$ populations, DOX activity is dominated by direct drug diffusion rather than receptor-mediated internalization.

3.5. *Confocal microscopy and Raman spectroscopy analysis*

Confocal fluorescence microscopy was employed to visualize the intracellular distribution of DOX and assess the localization of the GO@PEG–HA–DOX nanostructures in HT-1080 and SKBR3 cells after 24 h of incubation. Cell membranes were stained with CellMask Deep

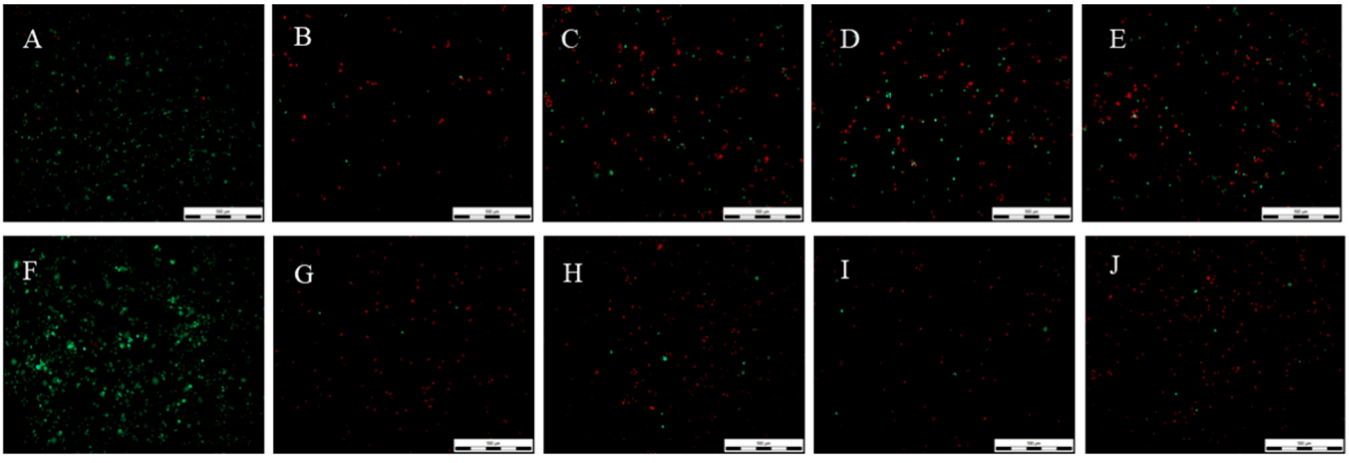

Fig. 6. Live/Dead fluorescence assay of HT-1080 and SKBR3 cells after 72 h of incubation. The control represents untreated cells, while all other samples were exposed to DOX administered either freely or within the GO@PEG–HA nanostructures, at a constant concentration of 15 μM. For HT-1080 cells: (A) control, (B) free DOX, (C) GO@PEG–$HA_{0.1}$–DOX, (D) GO@PEG–HA_1–DOX, and (E) GO@PEG–HA_{10}–DOX. For SKBR3 cells: (F) control, (G) free DOX, (H) GO@PEG–$HA_{0.1}$–DOX, (I) GO@PEG–HA_1–DOX, and (J) GO@PEG–HA_{10}–DOX. Green fluorescence (Calcein-AM) indicates metabolically active, viable cells, whereas red fluorescence (propidium iodide) marks membrane-compromised, dead cells. Scale bar: 500 μm.

Red (green channel) and nuclei with Hoechst 33342 (blue channel), while the inherent red fluorescence of DOX enabled direct observation of its intracellular distribution without additional labeling (Figs. 7 and 8).

In control cells (Fig. 7A), only membrane and nuclear staining were detected, confirming the absence of DOX fluorescence. All treated samples (Fig. 7B–D) exhibited clear red fluorescence, indicating intracellular accumulation of DOX. However, the fluorescence intensity and its subcellular localization differed depending on the HA concentration and the cell line.

At the lowest HA concentration (0.1 mg/mL), the red fluorescence was diffusely distributed throughout the cytoplasm, suggesting partial DOX release from the carrier and its passive diffusion across the plasma membrane. In contrast, at HA concentrations of 1 and 10 mg/mL, the red signal became more localized around the nuclei, forming discrete punctate structures consistent with endocytic vesicles typically observed during CD44-mediated internalization of HA-functionalized nanocarriers [36].

In HT-1080 cells, which overexpress CD44 receptors, the red signal was markedly stronger and concentrated in the perinuclear region compared to SKBR3 cells. This pattern supports receptor-mediated endocytosis and efficient intracellular accumulation of the nanocarrier system [37,38]. In some HT-1080 cells treated with GO@PEG–HA$_{10}$–DOX, partial overlap of red and blue fluorescence was observed, suggesting limited nuclear entry of DOX, consistent with its DNA intercalation properties [39]. In contrast, SKBR3 cells displayed weaker and more diffuse fluorescence, reflecting lower uptake efficiency due to limited CD44-mediated internalization.

While confocal microscopy confirmed the intracellular presence of DOX, the inherent fluorescence of the drug alone does not allow distinction between free DOX released from the carrier and intact GO@PEG–HA–DOX nanocomplexes. To resolve this ambiguity, Raman spectroscopy was employed as a complementary, label-free technique capable of directly detecting the carbon-based nanocarrier.

Raman mapping of individual HT-1080 (Fig. 9A–B) and SKBR3 (Fig. 9C–D) cells revealed distinct D (~1350 cm^{-1}) and G (~1590 cm^{-1}) bands characteristic of graphene oxide at positions corresponding to regions of red fluorescence in the confocal images (Spot 1) [34,35]. Spectra collected from adjacent cytoplasmic areas without red fluorescence (Spot 2) showed only biomolecular signals from proteins and lipids (~2850–3000 cm^{-1}). The co-localization of graphene oxide Raman peaks with DOX fluorescence thus provides direct evidence that the entire GO@PEG–HA–DOX nanoplatform penetrates the cells, rather than only the released DOX molecules.

Raman signal intensity reflects local nanocarrier accumulation and focal signal enhancement rather than absolute intracellular

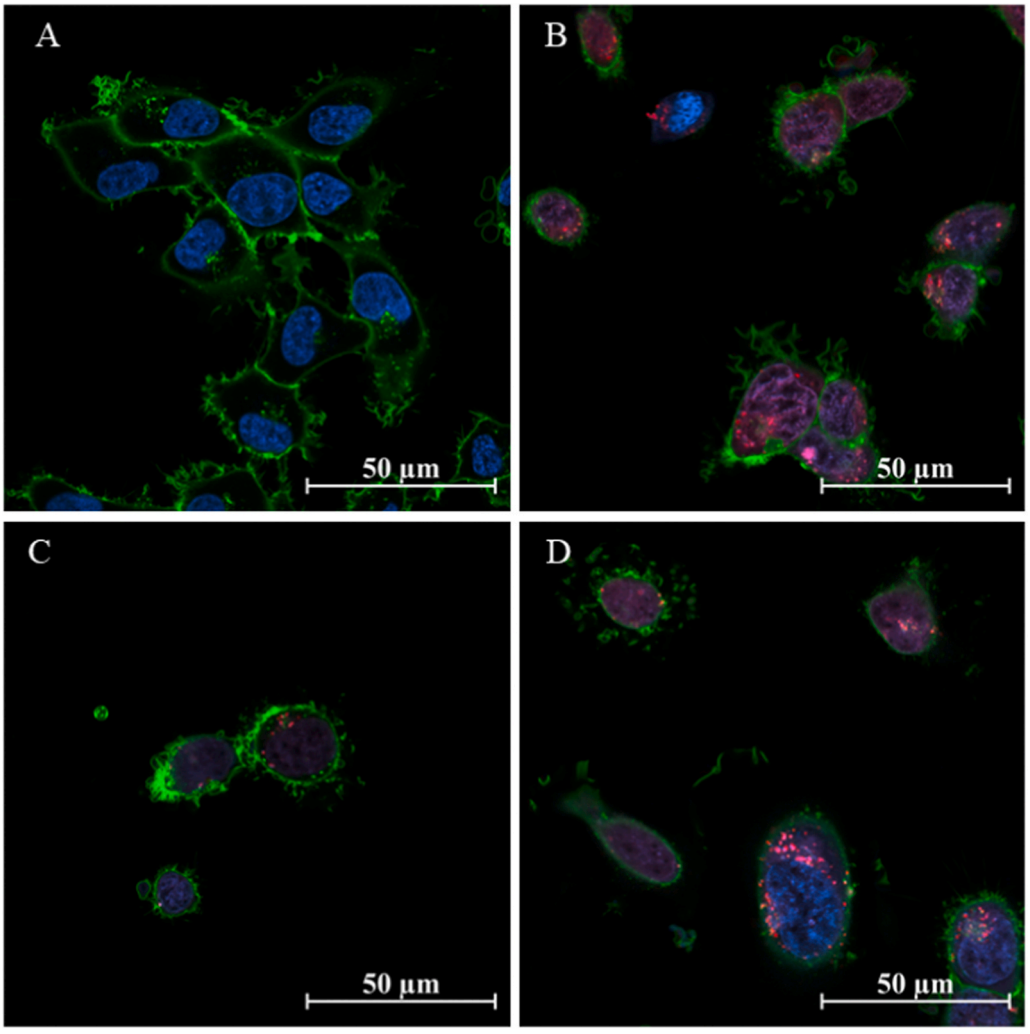

Fig. 7. Confocal fluorescence microscopy of HT-1080 cells after 24 h of incubation. Confocal fluorescence images showing the intracellular localization of GO@PEG–HA–DOX nanostructures in CD44-overexpressing HT-1080 cells. Cell membranes were stained with CellMask Deep Red (green channel), nuclei with Hoechst 33342 (blue channel), and DOX fluorescence was visualized through its inherent red emission. Images correspond to: (A) control (untreated cells), (B) GO@PEG–HA$_{0.1}$–DOX, (C) GO@PEG–HA$_1$–DOX, and (D) GO@PEG–HA$_{10}$–DOX; all samples were tested at a final DOX concentration of 2 µM. Scale bar: 50 µm.

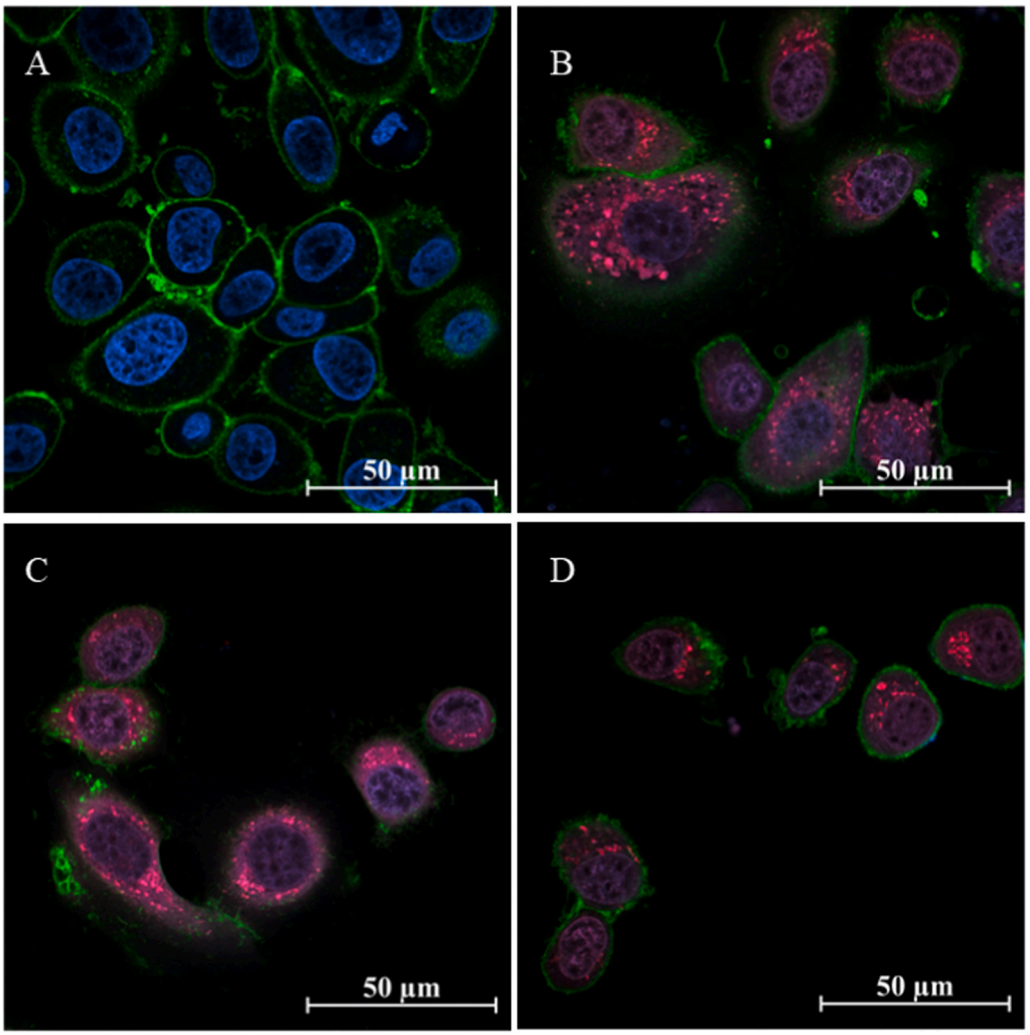

Fig. 8. Confocal fluorescence microscopy of SKBR3 cells after 72 h of incubation. Confocal fluorescence images of SKBR3 cells treated under identical conditions as HT-1080. (A) control, (B) GO@PEG–$HA_{0.1}$–DOX, (C) GO@PEG–HA_{1}–DOX, and (D) GO@PEG–HA_{10}–DOX; all samples were tested at a final DOX concentration of 2 μM. Scale bar: 50 μm.

concentration. Variations in cellular morphology, focal volume, and local aggregation can influence the intensity of the D and G bands. Therefore, Raman mapping was interpreted in conjunction with confocal microscopy and biological assays to assess intracellular localization and uptake trends rather than as a standalone quantitative measure.Furthermore, differences in Raman D/G band intensity were observed between HT-1080 and SKBR3 cells. When interpreted in the context of confocal microscopy and cytotoxicity data, these findings are consistent with more efficient nanocarrier internalization in $CD44^+$ HT-1080 cells mediated by CD44–HA interactions. This correlation between confocal fluorescence and Raman spectra verifies that DOX fluorescence within the cytoplasm and perinuclear regions originates from internalized GO@PEG–HA–DOX complexes, which subsequently release the drug intracellularly.

Taken together, the combined confocal and Raman analyses provide strong evidence that the GO@PEG–HA–DOX nanoplatform enters tumor cells as an intact complex through CD44-mediated endocytosis, followed by localized DOX release within the cell. The complementary use of fluorescence imaging and vibrational spectroscopy thus offers a powerful strategy for elucidating intracellular behavior of multifunctional nanocarriers and validating receptor-targeted delivery mechanisms.

4. Conclusions

In this work, a hyaluronic acid-functionalized PEGylated graphene oxide nanoplatform was developed for CD44 receptor-mediated intracellular delivery of doxorubicin in vitro. The nanocarrier was thoroughly characterized and its biological performance was evaluated using two cancer cell lines with distinct CD44 expression levels. Combined confocal microscopy and Raman spectroscopy confirmed intracellular localization of the nanoplatform and supported receptor-driven selectivity.

The present study is subject to certain limitations. In particular, extracellular drug release kinetics and comprehensive physicochemical optimization were not addressed, as the primary focus was placed on mechanistic evaluation of receptor-mediated cellular uptake and intracellular drug delivery.

Despite these limitations, the results provide a robust proof-of-concept for CD44-targeted nanocarrier-mediated drug delivery. The findings highlight the potential of graphene oxide-based multifunctional platforms for receptor-guided therapeutic strategies and establish a foundation for further investigation of such systems under more complex biological conditions.

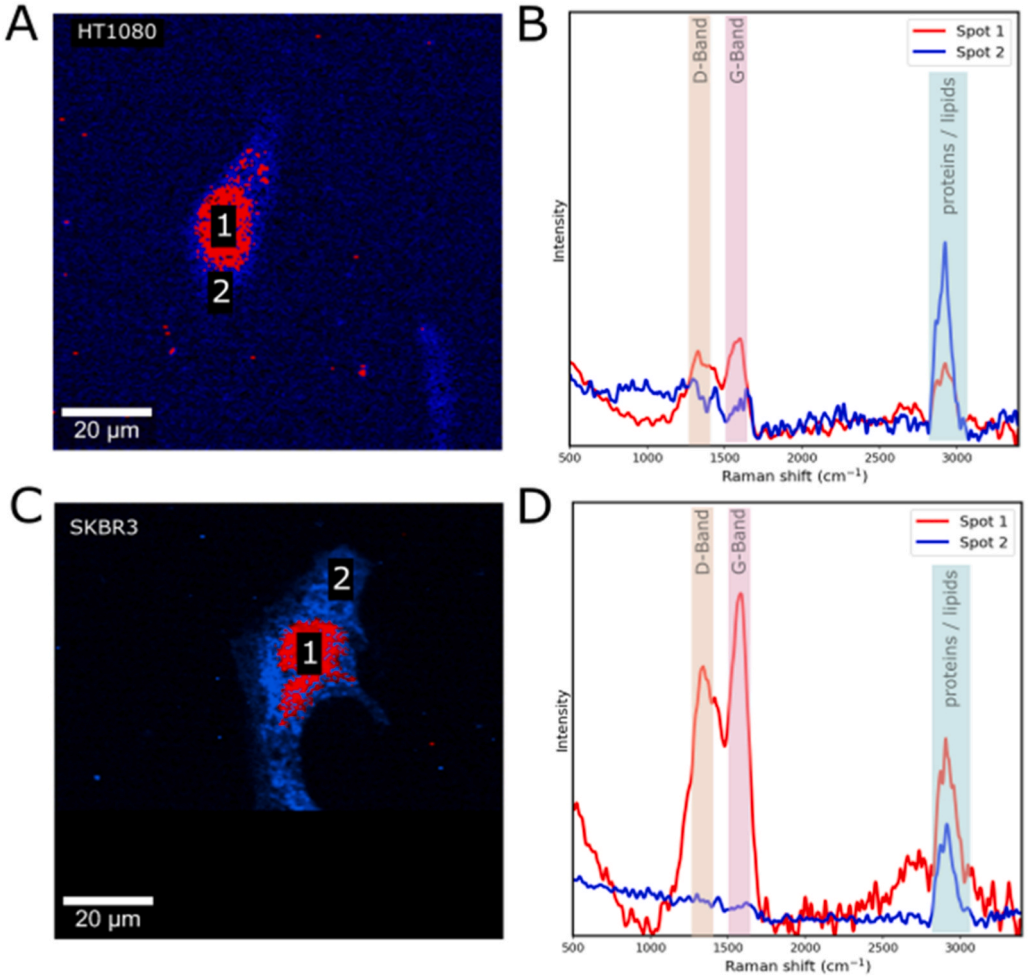

Fig. 9. Intracellular localization of GO@PEG–HA–DOX nanoplatforms analyzed by confocal microscopy and Raman spectroscopy. (A, B) HT-1080 ($CD44^+$) cells: (A) confocal fluorescence images showing intracellular DOX localization (red) and nuclei (blue); (B) corresponding Raman maps and spectra acquired from intracellular regions with DOX fluorescence (Spot 1) and adjacent cytoplasmic regions without fluorescence (Spot 2).(C, D) SKBR3 ($CD44^-$) cells: (C) confocal fluorescence images and (D) corresponding Raman maps and spectra acquired under the same conditions as for HT-1080 cells. Raman spectra display characteristic D (~1350 cm^{-1}) and G (~1590 cm^{-1}) bands GO.

CRediT authorship contribution statement

Ludmila Žárská: Writing – original draft, Investigation, Formal analysis, Data curation. **Zuzana Chaloupková:** Visualization, Validation, Methodology, Formal analysis, Data curation. **Michaela Gapčová:** Formal analysis, Data curation. **Václav Ranc:** Writing – review & editing, Supervision, Conceptualization.

Funding

This work has been funded by ERDF/ESF project TECHSCALE (No. CZ.02.01.01/00/22_008/0004587; The work was supported by the MEYS CR (Large RI Project LM2018129 Czech-BioImaging) and by the project National Institute for Cancer Research (Programme EXCELES, ID Project No. LX22NPO5102)—Funded by the European Union—Next Generation EU, project SALVAGE (OP JAC; reg. no. CZ.02.01.01/00/22_008/0004644).

Declaration of Competing Interest

The authors declare that they have no known competing financial interests or personal relationships that could have appeared to influence the work reported in this paper.

Acknowledgments

None.

Appendix A. Supporting information

Supplementary data associated with this article can be found in the online version at doi:10.1016/j.biopha.2026.119036.

Data availability

Data will be made available on request.

References

[1] I. Dagogo-Jack, A.T. Shaw, Tumour heterogeneity and resistance to cancer therapies, Nat. Rev. Clin. Oncol. 15 (1) (2018) 81–94, https://doi.org/10.1038/nrclinonc.2017.166.
[2] H. Jin, L. Wang, R. Bernards, Rational combinations of targeted cancer therapies: background, advances and challenges, Nat. Rev. Drug Discov. 22 (2023) 213–234, https://doi.org/10.1038/s41573-022-00615-z.
[3] B. Liu, H. Zhou, L. Tan, et al., Exploring treatment options in cancer: tumor treatment strategies, Signal Transduct. Target Ther. 9 (2024) 175, https://doi.org/10.1038/s41392-024-01856-7.
[4] M.I. Khan, M.I. Hossain, M.K. Hossain, et al., Recent progress in nanostructured smart drug delivery systems for cancer therapy: a review, ACS Appl. Bio Mater. 5 (3) (2022) 971–1012, https://doi.org/10.1021/acsabm.2c00002.

[5] M.T. Manzari, Y. Shamay, H. Kiguchi, et al., Targeted drug delivery strategies for precision medicines, Nat. Rev. Mater. 6 (2021) 351–370, https://doi.org/10.1038/s41578-020-00269-6.
[6] E.V. Emeihe, E.I. Nwankwo, M.D. Ajegbile, et al., Revolutionizing drug delivery systems: nanotechnology-based approaches for targeted therapy, Int. J. Life Sci. Res. Arch. 7 (1) (2024) 40–58, https://doi.org/10.53771/ijlsra.2024.7.1.0060.
[7] S. Kunjiappan, P. Pavadai, S. Vellaichamy, et al., Surface receptor-mediated targeted drug delivery systems for enhanced cancer treatment: a state-of-the-art review, Drug Dev. Res. 82 (2021) 309–340, https://doi.org/10.1002/ddr.21758.
[8] J. Georgeous, N. AlSawaftah, W.H. Abuwatfa, et al., Review of gold nanoparticles: synthesis, properties, shapes, cellular uptake, targeting, release mechanisms and applications in drug delivery and therapy, Pharmaceutics 16 (2024) 1332, https://doi.org/10.3390/pharmaceutics16101332.
[9] A. Kumar, S.S. Das, S. Tambe, et al., Unravelling the potential role of polyethyleneimine (PEI)-based nanosystems in skin cancer therapy, Mater. Adv. (2025), https://doi.org/10.1039/D4MA00802B.
[10] D. Yadav, H.K. Dewangan, PEGYLATION: an important approach for novel drug delivery system, J. Biomater. Sci. Polym. Ed. 32 (2) (2020) 266–280, https://doi.org/10.1080/09205063.2020.1825304.
[11] E. Sanchez Armengol, A. Unterweger, F. Laffleur, PEGylated drug delivery systems in the pharmaceutical field: past, present and future perspective, Drug Dev. Ind. Pharm. 48 (4) (2022) 129–139, https://doi.org/10.1080/03639045.2022.2101062.
[12] J.R.M.H. Al-Shadidi, Z. Hussain, I. Ahmed, et al., Polyethylene glycol-mediated functionalization of nanodelivery systems for improving their pharmacokinetic profile and anticancer efficacy, Int. J. Polym. Mater. Polym. Biomater. (2024) 1–19, https://doi.org/10.1080/00914037.2024.2383413.
[13] M. Kciuk, A. Gielecińska, S. Mujwar, D. Kołat, Ż. Kałuzińska-Kołat, I. Celik, R. Kontek, Doxorubicin—an agent with multiple mechanisms of anticancer activity, Cells 12 (2023) 659, https://doi.org/10.3390/cells12040659.
[14] M. Zhao, X. Zhang, D. Zhou, J. Song, Advancements in managing anthracycline-induced cardiotoxicity: insights from interventional clinical trials, Open Access J. Clin. Trials 17 (2025) 1–14, https://doi.org/10.1080/14737140.2021.1991316.
[15] P. Kesharwani, R. Chadar, A. Sheikh, et al., CD44-targeted nanocarrier for cancer therapy, Front. Pharm. 12 (2021) 800481, https://doi.org/10.3389/fphar.2021.800481.
[16] Z. Hussain, A.H. Akbari, S.H. Barbuor, et al., Hyaluronic acid-based functionalization of nanodelivery systems: a promising strategy for CD44 receptor-mediated targeted therapy of lung cancer, J. Drug Deliv. Sci. Technol. 101 (2024) 106183, https://doi.org/10.1016/j.jddst.2024.106183.
[17] M. Li, J. Sun, W. Zhang, et al., Drug delivery systems based on CD44-targeted glycosaminoglycans for cancer therapy, Carbohydr. Polym. 251 (2021) 117103, https://doi.org/10.1016/j.carbpol.2020.117103.
[18] N. Cirillo, The hyaluronan/CD44 axis: a double-edged sword in cancer, Int. J. Mol. Sci. 24 (2023) 15812, https://doi.org/10.3390/ijms242115812.
[19] X. Ma, H. Tao, K. Yang, et al., Nano Res. 5 (2012) 199–208, https://doi.org/10.1007/s12274-012-0200-y.
[20] J. Chen, H. Liu, C. Zhao, et al., Biomaterials 35 (2014) 4986–4994, https://doi.org/10.1016/j.biomaterials.2014.02.032.
[21] I. Jung, M. Pelton, R. Piner, et al., Simple approach for high-contrast optical imaging and characterization of graphene-based sheets, Nano Lett. 7 (2007) 3569–3575, https://doi.org/10.1021/nl0714177.
[22] E. Giusto, L. Žárská, D.F. Beirne, et al., Graphene oxide nanoplatforms to enhance cisplatin-based drug delivery in anticancer therapy, Nanomaterials 12 (2022) 2372, https://doi.org/10.3390/nano12142372.
[23] L. Žárská, V. Ranc, Dual drug delivery in cancer therapy using graphene oxide-based nanoplatforms, Adv. Nano Biomed. Res. 4 (2024) 2400026, https://doi.org/10.1002/anbr.202400026.
[24] I. Tufano, R. Vecchione, P.A. Netti, Methods to scale down graphene oxide size and size implication in anti-cancer applications, Front. Bioeng. Biotechnol. 8 (2020) 613280, https://doi.org/10.3389/fbioe.2020.613280.
[25] Z. Guo, S. Chakraborty, F.A. Monikh, et al., Surface functionalization of graphene-based materials: biological behavior, toxicology, and future perspectives, Adv. Biol. 5 (11) (2021) 2100637, https://doi.org/10.1002/adbi.202100637.
[26] N. Bellier, P. Baipaywad, N. Ryu, et al., Recent biomedical advancements in graphene oxide- and reduced graphene oxide-based nanocomposite nanocarriers, Biomater. Res. 26 (2022) 65, https://doi.org/10.1186/s40824-022-00313-2.
[27] J. Chen, X. Wang, T. Chen, Facile and green reduction of covalently PEGylated nanographene oxide via a "water-only" route for high-efficiency photothermal therapy, Nanoscale Res. Lett. 9 (2014) 86, https://doi.org/10.1186/1556-276X-9-86.
[28] P. Bolibok, B. Szymczak, K. Roszek, et al., A new approach to obtaining nano-sized graphene oxide for biomedical applications, Materials 14 (2021) 1327, https://doi.org/10.3390/ma14061327.
[29] G. Ruggiero, D. Di Rosa, F. Caso, et al., Synthesis and FT-IR/Raman characterization of a graphene oxide–methacrylamide monomer for dental applications, Materials 18 (2025) 3550, https://doi.org/10.3390/ma18153550.
[30] C.-P. Fu, X.-Y. Cai, S.-L. Chen, H.-W. Yu, Y. Fang, X.-C. Feng, L.-M. Zhang, C.-Y. Li, Hyaluronic acid-based nanocarriers for anticancer drug delivery, Polymers 15 (2023) 2317, https://doi.org/10.3390/polym15102317.
[31] T.H. Akere, A.M.Z. de Medeiros, D.S.T. Martinez, et al., Synthesis and characterisation of a graphene oxide–gold nanohybrid for use as test material, Nanomaterials 11 (2021) 1278, https://doi.org/10.3390/nano11051278.
[32] M. Szota, B. Jachimska, Effect of alkaline conditions on forming an effective G4.0 PAMAM complex with doxorubicin, Pharmaceutics 15 (2023) 875, https://doi.org/10.3390/pharmaceutics15030875.
[33] Z. Liu, J.T. Robinson, X. Sun, H. Dai, PEGylated nanographene oxide for delivery of water-insoluble cancer drugs, ACS Nano 2 (11) (2008) 393–396, https://doi.org/10.1021/nn800258c.
[34] A.C. Ferrari, J. Robertson, Interpretation of Raman spectra of disordered and amorphous carbon, Phys. Rev. B 61 (20) (2000) 14095–14107, https://doi.org/10.1103/PhysRevB.61.14095.
[35] S. Stankovich, D.A. Dikin, R.D. Piner, et al., Synthesis of graphene-based nanosheets via chemical reduction of exfoliated graphite oxide, Carbon 45 (2007) 1558–1565, https://doi.org/10.1016/j.carbon.2007.02.034.
[36] D. Peer, J.M. Karp, S. Hong, et al., Nanocarriers as an emerging platform for cancer therapy, Nat. Nanotechnol. 2 (2007) 751–760, https://doi.org/10.1038/nnano.2007.387.
[37] K.Y. Choi, G. Saravanakumar, J.H. Park, K. Park, Hyaluronic acid-based nanocarriers for intracellular targeting: interfacial interactions with proteins in cancer, Colloids Surf. B Biointerfaces 99 (2012) 82–94, https://doi.org/10.1016/j.colsurfb.2011.10.029.
[38] J.M. de la Rosa, P. Pingrajai, M. Pelliccia, et al., Binding and internalization in receptor-targeted carriers: the complex role of CD44 in the uptake of hyaluronic acid-based nanoparticles, Adv. Healthc. Mater. 8 (24) (2019) e1901182, https://doi.org/10.1002/adhm.201901182.
[39] G. Minotti, P. Menna, E. Salvatorelli, et al., Anthracyclines: molecular advances and pharmacologic developments, Pharmacol. Rev. 56 (2) (2004) 185–229, https://doi.org/10.1124/pr.56.2.6.